Effect of a New High-Pressure Heat Treatment on Additively Manufactured AlSi10Mg Alloy

MARIALAURA TOCCI, ANNALISA POLA, MARCELLO GELFI,
and GIOVINA MARINA LA VECCHIA

The application of an innovative high-pressure T6 treatment (HPT6) to additively manufactured AlSi10Mg alloy is reported in this paper. The aim of this treatment is to obtain the effective densification of the material together with the hardening effects typical of T6 heat treatment in one step. For comparison, a two-step treatment consisting of hot isostatic pressing followed by conventional T6 treatment was applied. Standard annealing and T6 treatment alone were also considered. The microstructural and mechanical properties of alloys treated under all the studied conditions were analyzed and their density was measured to quantify their densification. Although the application of high pressure hindered the diffusion mechanisms, and thus could limit the hardening effect of heat treatment, HPT6 treatment was found to ensure suitable mechanical properties and high densification. Furthermore, it required less time; therefore, it can be considered as a time-efficient process for high-performance applications.

https://doi.org/10.1007/s11661-020-05905-y

I. INTRODUCTION

ADDITIVE manufacturing (AM) is an innovative and expanding technology for the industrial production of prototypes and small series of metallic components. It is applied primarily in the aerospace, medical, health care, automotive, and energy industries, but the market for additively manufactured parts in other sectors, such as artistic and architectural models, sporting goods, and entertainment props, is also increasing.

Various alloys can be used in metal AM, such as alloys based on stainless steel, titanium, nickel, cobalt–chromium, and aluminum and, more recently, copper and magnesium alloys and precious metals.[1–8] Among them, aluminum alloys are attracting wide interest, thanks to the combination of good properties, low density, and reasonable cost of the powders.[9] In this family, the alloys that have shown promising results in terms of processability by AM are generally cast alloys, such as AlSi10Mg and AlSi12, because of their small solidification range and low shrinkage due to the eutectic phase. In particular, as-built AlSi10Mg shows remarkable mechanical properties[10,11] because of its ultrafine microstructure characterized by the cellular α-Al phase and fibrous Si particles resulting from the very high cooling rates typical of the AM process.[12,13] A356, A357, and Al-Mg-Sc alloys have also been applied recently in some additively manufactured components,[14–16] and new Al alloys suitable for AM are being designed.[17]

In addition, many researchers have also attempted to improve the properties of additively manufactured parts by enhancing their quality, *i.e.*, by reducing defects such as gas and lack-of-fusion porosities.[18] Their formation during laser-based powder bed fusion processes is well documented in the literature.[19] The former are due to entrapment of gas in the material during solidification. Indeed, argon in the building chamber can be trapped in the material, as well as hydrogen or other gases contained in internal pores of the raw metal powders, as vaporization of volatile elements causes moisture or gas to form during solidification.[20] Furthermore, studies have demonstrated that Marangoni flow and convection phenomena support hydrogen enrichment of the molten metal and trap the pores within the melt pool, increasing the risk of pore formation.[20,21] Lack-of-fusion defects are due to suboptimal processing parameters that result in the incomplete melting of the powder during construction, with consequent poor overlap of the melt pools. They have irregular shapes, whereas gas pores are spherical. Additionally, the alignment of these defects (parallel or perpendicular) to the tensile axis, which depends on the part-building orientation, significantly affects the mechanical performance of additively manufactured parts, further increasing their anisotropic behavior.[22] Note that the volume fraction of porosity is

---

MARIALAURA TOCCI, ANNALISA POLA, MARCELLO GELFI, and GIOVINA MARINA LA VECCHIA are with the Department of Mechanical and Industrial Engineering, University of Brescia, via Branze 38, 25123 Brescia, Italy. Contact e-mail: marialaura.tocci@unibs.it

Manuscript submitted March 9, 2020.

usually quite low (frequently less than 0.5 pct[23]); however, the large number of such pores encourages crack initiation under a fatigue load, thus degrading the performance of additively manufactured components.

Therefore, metal AM products undergo post-treatments such as hot isostatic processing (HIP) to increase their density.[24,25] For aluminum alloys, this treatment is usually performed at temperatures above 500 °C and in Ar atmosphere under pressure, typically 75–150 MPa.[22,24,26–28] This reduces the porosity and increases the ductility and toughness, but at the cost of decreasing the hardness, strength, and fatigue resistance, as reported by many authors.[22,27,29] This is a consequence of the modification of the ultrafine microstructure typical of the as-built alloy into a coarser one characterized by rounded silicon particles in the Al matrix, similar to the microstructure of an alloy subjected to T6 treatment (solution treatment, quenching, and artificial aging).[22] Moreover, in contrast to heat-treated alloys that experience similar thermal conditions, no aging occurs after cooling from the HIP temperature, because the cooling rate is usually too low to obtain a supersaturated solid solution of Mg and Si.[30] Consequently, it is necessary to perform a complete T6 treatment after HIP to obtain the desired mechanical properties.[13,24] However, different authors have noted that the pores closed by HIP can progressively re-open and grow during T6 treatment; moreover, oxides can form at the HIP temperature.[9,23,31] In addition, some pores can appear closed after HIP even though a certain discontinuity between the pore walls remains (so called kissing bonds). This kind of two-dimensional defects are difficult to be identified and can represent a critical point for stress concentration during loading. Pore enlargement during T6 treatment is likely because of the high pressure within the pores remaining after HIP as a consequence of the low diffusivity of Ar in the aluminum lattice,[28] combined with the reduced resistance to the deformation of the alloy at high temperatures.

A possible solution to this pore expansion is to use HIP as a solution treatment performed under pressure and follow it directly with rapid quenching and subsequent aging, both of which are performed in the HIP vessel. This innovative heat treatment, combining in a single step HIP and T6, should ensure the formation of hardening precipitates, avoiding the risk that pores re-open because of the pressure applied during solution treatment and quenching, which is performed using pressurized cold gas.[32]

Note that a pressure of 100 MPa can cause an increase of approximately 4 °C in the eutectic temperature of the Al–Si system, as calculated by ThermoCalc software. Therefore, the temperature maintained during HIP is significantly below the temperature of eutectic melting, but it is sufficiently high to guarantee Si solubility. For the Al-Mg-Si system, the temperature of HIP treatment is not close to the solidus line, and it can be assumed that it is also sufficiently above the solvus line to ensure diffusion of Mg even at high pressure.

Moreover, as reported by Hafenstein *et al.*[30] for cast Al-Si-Mg alloy, the high pressure during HIP affects the oversaturation of alloying elements by decreasing the diffusivity of Mg and Si atoms in the Al matrix. This also reduces the critical cooling rate at which an oversaturated solution can be obtained. Therefore, the cooling conditions that can be obtained in the HIP vessel can be sufficient to produce a saturated solution of Si and Mg atoms after HIP so that aging can be performed immediately afterward without a separate solution treatment, thus reducing the lead time, cost, and capital investment.

In this paper, the effects of this innovative route on the mechanical properties of additively manufactured AlSi10Mg alloy are investigated, and the results are compared with those of conventional annealing, T6 treatment, and HIP followed by T6 treatment. In particular, hardness and quasi-static tensile strength were investigated and the results were correlated with microstructural features from deep metallographic analysis.

II. MATERIALS AND METHODS

Samples were produced by a laser powder bed fusion technique using a SLM 500 system in high purity Ar atmosphere. The layer thickness was 50 μm, and the platform was heated at 150 °C. Because a company produced the samples, the other processing parameters are confidential and cannot be specified, as reported in other scientific research performed in collaboration with industry.[22] However, the same process parameters were used to build all the samples tested in this study. This allows consistent evaluation of the effect of the various heat treatment routes, which is the aim of the study, even though the laser parameters are not reported.

Cubic samples (12 × 12 × 12 mm^3) and tensile samples with a diameter of 6 mm in the gauge length region were produced (gauge length of 25 mm). Tensile samples were built in both the vertical and horizontal directions. In this study, five cubic samples and thirty tensile samples (fifteen for each building orientation) were used. An image representative of the shape of the samples is visible in Figure 1.

The chemical composition of the studied alloy is provided in Table I.

The samples were then heat-treated by four different routes to evaluate their effects. The four heat treatments, denoted as annealing, T6 treatment, HIP + T6 treatment, and HPT6 treatment (the new high-pressure T6 treatment), are illustrated in Figure 2. One cubic sample

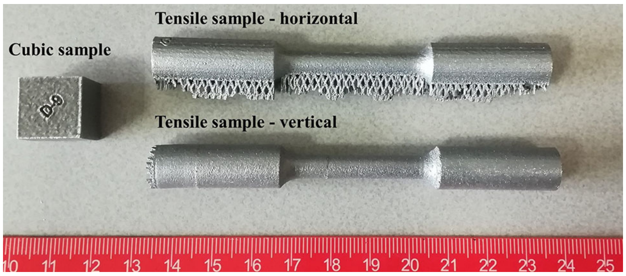

Fig. 1—Shape of samples used in the present study.

and six tensile specimens (three built in horizontal and three built in vertical direction) were used for each heat treatment route.

Conventional annealing and T6 treatment were conducted in laboratory furnaces. Annealing was performed at 300 ± 1 °C for 2 hours, typical conditions reported in the literature.[33] The heating rate was 15 °C/min, while after annealing, samples cooled down in air.

In the T6 treatment, samples were solution heat-treated at 520 ± 2 °C for 2 hours, water quenched at 65 °C to ensure optimal quenching conditions,[34] and immediately aged at 165 ± 1 °C for 4 hours.

As mentioned, HIP + T6 treatment was performed to reduce the porosity, which typically increases after T6 treatment. Specifically, HIP was performed at 520 °C for 2 hours at 150 MPa in Argon in a Quintus Technologies HIP machine. This was followed by T6 treatment in laboratory furnaces at atmospheric pressure with the time and temperature parameters described above.

Table I. Nominal Composition (Wt Pct) of the Studied Alloy

Si	Mg	Fe	Mn	Al
9–11	< 0.55	< 0.55	< 0.45	balance

Finally, the HPT6 heat treatment route was applied, as follows. At the end of HIP (520 °C for 2 hours at 150 MPa), samples were directly quenched inside the HIP vessel using a cooling gas and then reheated to the aging temperature of 165 °C for 4 hours while high pressure was maintained. Thus, the entire treatment was performed at high pressure (150 MPa). The working principles of the uniform rapid quenching unit are described in Reference 32. A recent study reported the application of this technology to an A356 alloy produced by gravity casting,[30] but it has not yet been applied to an additively manufactured Al alloy.

As-built and heat-treated cubic samples were machined to remove the external layer, and cubes with a final size of 10 × 10 × 10 mm^3 were obtained. As-built and heat-treated tensile samples were machined to the final shape according to the UNI EN ISO 6892-1 standard (sample diameter of 5 mm and gauge length of 25 mm).

After machining, the density of all the samples was measured by Archimedes' method using a weight scale (Gibertini Europe 500), as typically done to estimate the quality of AM parts.[31,35,36] The average and standard deviation were calculated. In this way, it was possible to compare the effect of HIP treatment on the density of the as-built, annealed, and T6-treated samples.

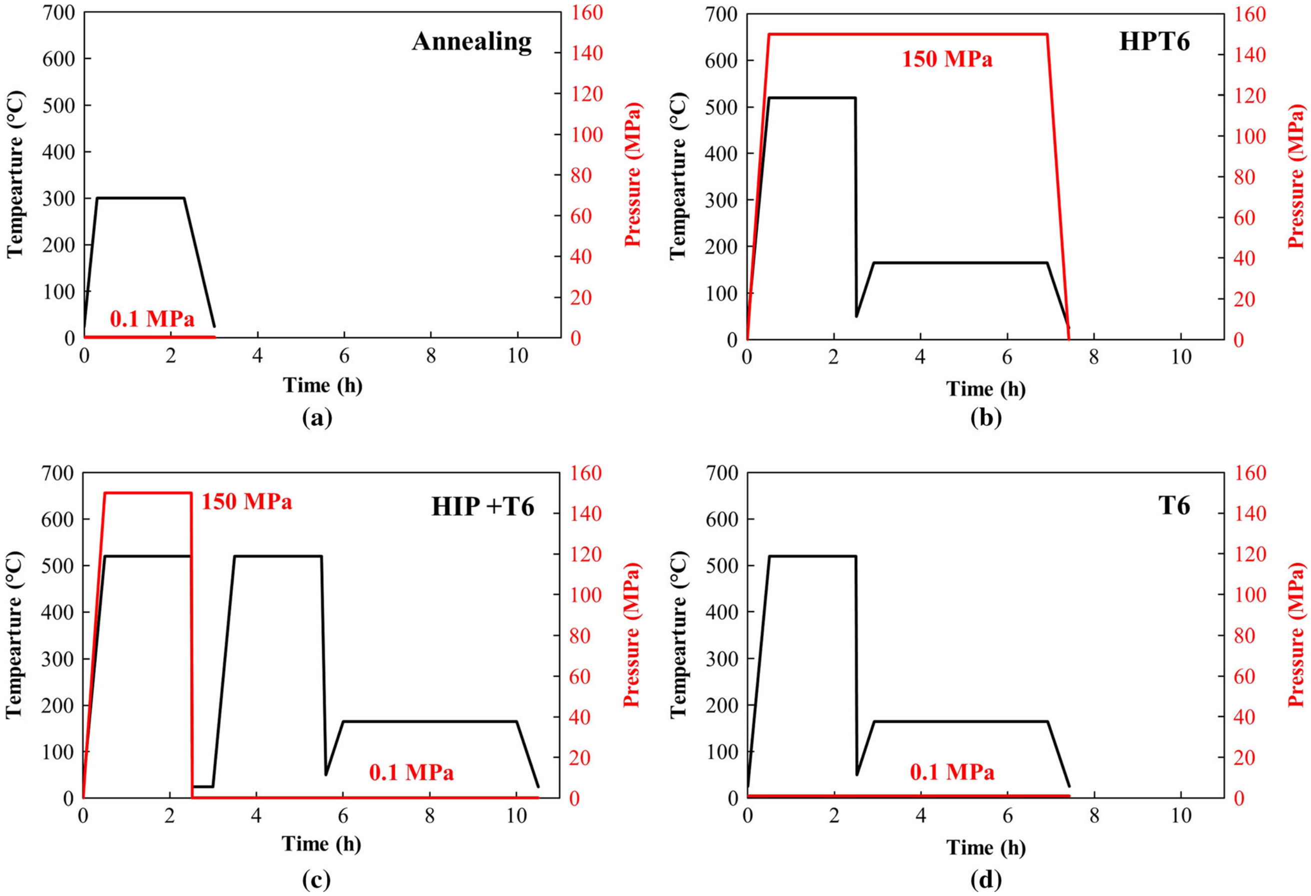

Fig. 2—Schematic representation of thermal and pressure cycles during (*a*) annealing, (*b*) HPT6, (*c*) HIP + T6, and (*d*) T6 treatments.

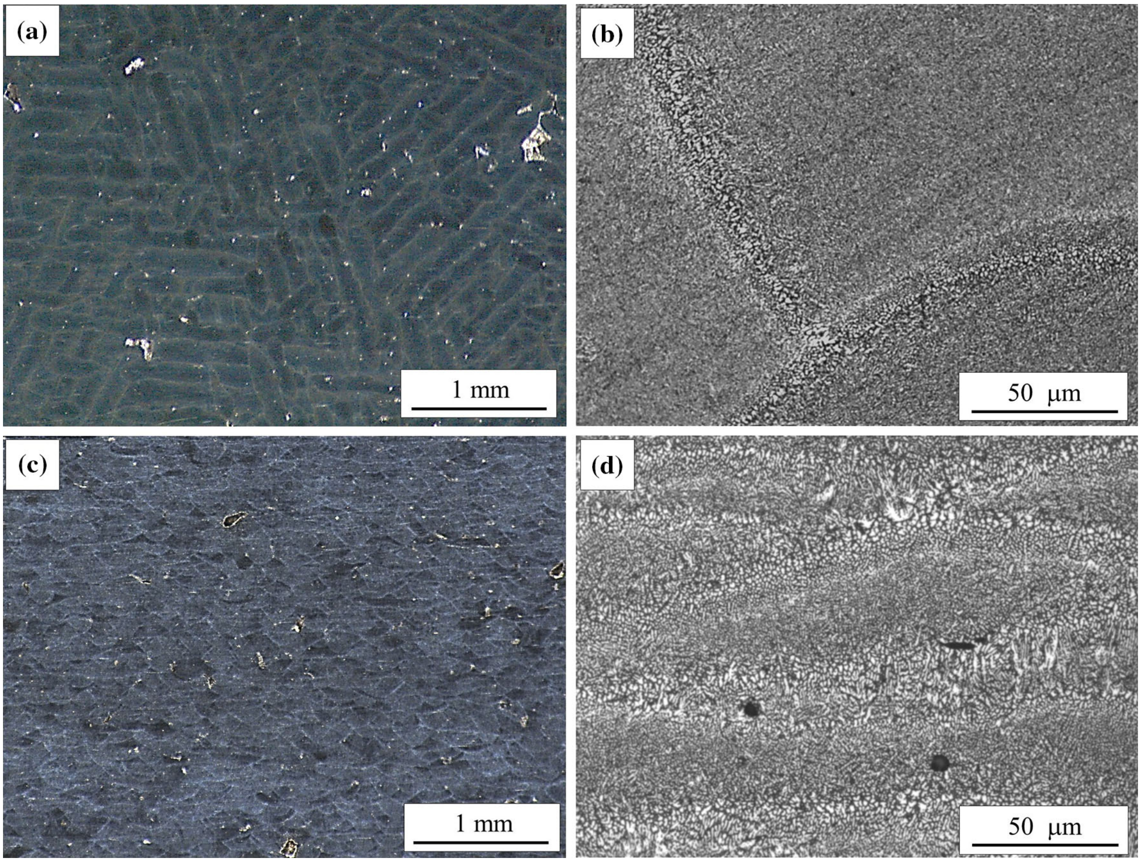

Fig. 3—Microstructure of the as-built sample along (*a*, *b*) *xy* and (*c*, *d*) *xz* planes.

Microstructural characterization and hardness measurements of the cubic samples were performed. The microstructure of the samples in each studied condition was observed by optical microscopy (LEICA DMI 500 M) and scanning electron microscopy (SEM, LEO EVO 40). In addition, as-built samples were also analyzed by digital microscopy (Leica 300) to study the scanning patterns on the *xy* and *xz* planes. Samples were observed after they were polished to a mirror finish by conventional metallographic procedures. In addition, as-built samples were etched with Keller reagent (1 pct HF, 1.5 pct HCl, and 2.5 pct HNO_3 in distilled water) for 30 seconds.

For samples treated under T6, HIP + T6, and HPT6 conditions, five digital images obtained at a magnification of 500 times were analyzed to determine the area fraction and density of Si particles. In addition, the area and equivalent diameter of these particles were statistically evaluated using JMP® software to assess the effect of high pressure on the diffusion of Si atoms and the consequent coarsening of Si particles during aging.

The Brinell hardness was measured using an LTF Galileo Ergotest Comp 25 testing machine by applying a load of 613 N for 15 seconds. The indenter was a tungsten carbide ball with a diameter of 2.5 mm. The measurement was repeated five times, and the average and standard deviation were calculated.

An Instron 3369 testing machine with a load cell of 50 kN was used for tensile tests. The elongation was measured using a knife edge extensometer fixed at the gauge length of the samples. The crosshead speed was set to 1 mm/min in the elastic field and 2 mm/min in the plastic field. Three samples were tested under each condition; the ultimate tensile strength (UTS), yield strength (YS), and elongation (El, pct) values were extrapolated from the strain–stress curves, and the average and standard deviation were calculated. The fracture surfaces were observed using a scanning electron microscope (LEO EVO 40) equipped with an Oxford energy-dispersive spectroscopy (EDS) probe for semi-quantitative elemental analysis.

III. RESULTS AND DISCUSSION

Figure 3 shows the microstructure of the studied material in the as-built condition. Figures 3(a) and (c) are obtained using a digital microscope. The horizontal cross-section (Figure 3(a)) shows the pattern followed by the laser (stripe-like scan tracks), whereas in the vertical cross-section, an irregular texture consisting of small semi-circular melt pools can be observed (Figure 3(c)). Figures 3(b) and (d), which were obtained at higher magnification by optical microscopy, show a

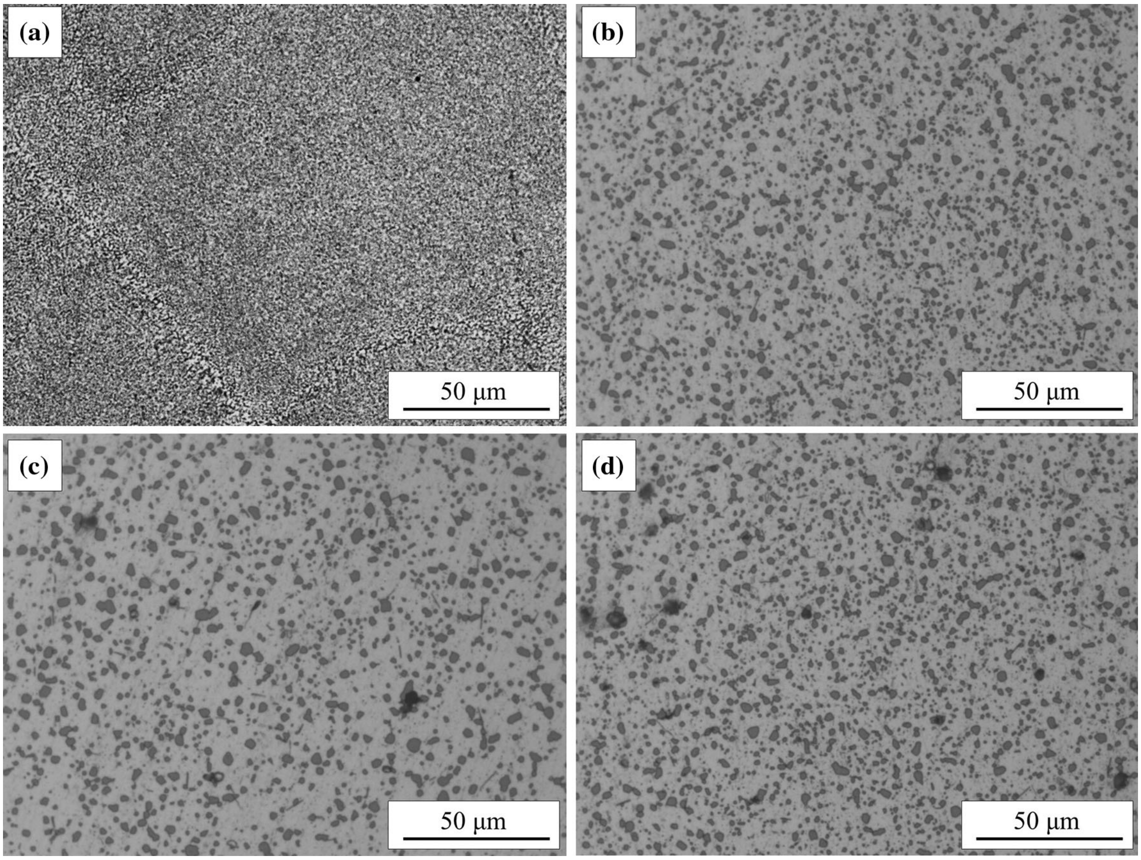

Fig. 4—Micrographs of vertical cross-section of samples after (*a*) annealing, (*b*) HPT6, (*c*) HIP + T6, and (*d*) T6 treatment.

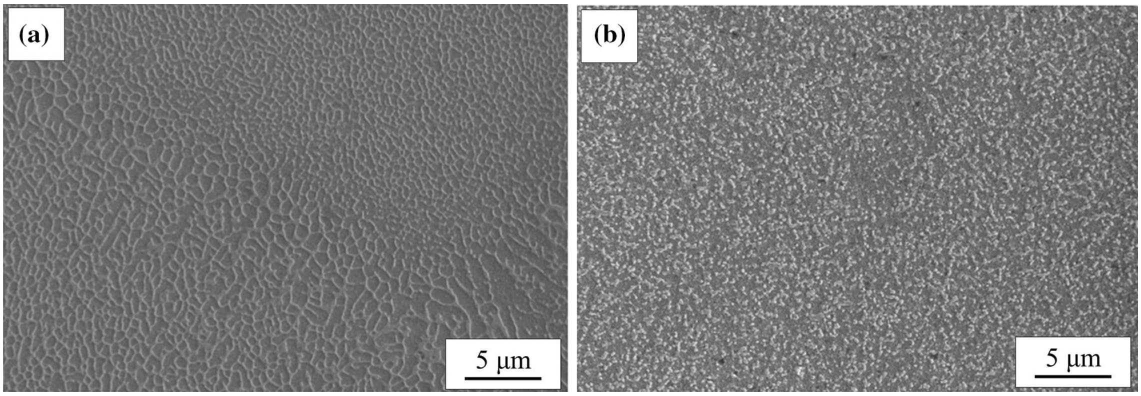

Fig. 5—SEM images of samples in (*a*) as-built and (*b*) annealed conditions.

fine network of Si particles in the Al matrix; this morphology is typical of this building process, which causes high cooling rates and thermal gradients in the melt pools.[11,37] This network is visibly coarser along the boundary of the melt pools (Figure 3(d)), where the alloy is reheated during melting and solidification of consecutive layers.[38] For this reason, the melt pool boundary represents a weak area under load conditions and a preferential path for fracture propagation.[25,39] Defects such as pores are also present in the microstructure, as shown in Figure 3(d).

Figure 4 shows the microstructure after each type of heat treatment. Annealing at 300 °C did not significantly modify the material microstructure, as the melt pool boundary can still be identified (Figure 4(a)), whereas the other heat treatments, which involved soaking at 520 °C, caused dramatic changes (Figures 4(b) through (d)). In particular, the coarsening of Si particles is the main consequence of the diffusion of Si atoms at the treatment temperature.[10] Note that the coarsening of Si particles, which is a diffusion-driven phenomenon, is affected by the duration, temperature, and pressure.

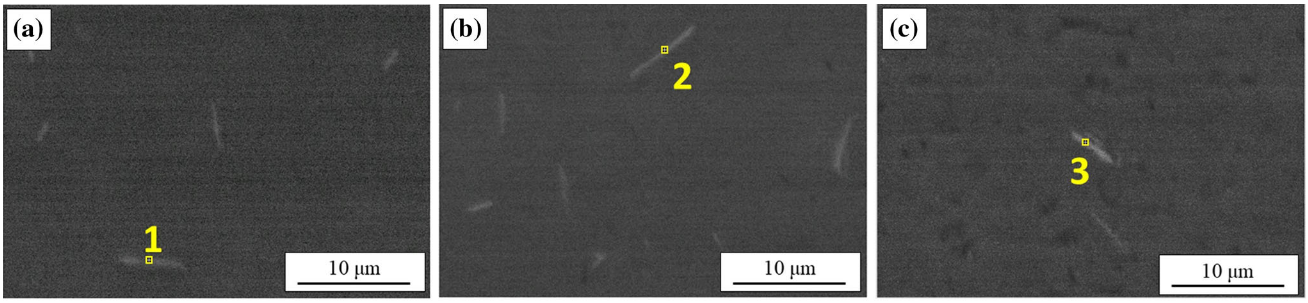

Spectrum	Al	Si	Fe
1	75.72	18.90	5.38

Spectrum	Al	Si	Fe
2	82.76	12.40	4.84

Spectrum	Al	Si	Fe
3	83.93	12.61	3.46

Fig. 6—Presence of Fe-bearing intermetallics in (*a*) HPT6, (*b*) HIP + T6, and (*c*) T6 samples: SEM images and corresponding EDS analysis (wt pct).

Therefore, the various applied heat treatments, which involve different pressure and durations, are expected to produce different material responses. In the micrographs of the HPT6, HIP + T6, and T6 samples (Figures 4(b) through (d)), no significant differences in Si particles size can be detected. However, this point was investigated in more detail by digital image analysis. In addition, as expected from the literature,[4,13] some pores are present in the sample after T6 treatment (Figure 4(d)), whereas these defects are less evident in the HIPed samples (Figures 4(b) and (c)). However, this is not sufficient to infer conclusions on the porosity level of the sample. Therefore, this point was investigated by measurements of the density of all the treated samples, as illustrated later.

SEM images for as-built and annealed samples (Figure 5) are helpful in identifying further microstructural features. Annealing at 300 °C (Figure 5(b)) is clearly responsible for the disintegration of the network of interconnected Si particles that appears in the as-built sample (Figure 5(a)), although the particles remain very fine, which is consistent with other studies.[40]

Furthermore, small needle-like particles containing Fe, which formed during heat treatment at high temperature, were identified in the HPT6, HIP + T6, and T6 samples (Figure 6), and were also reported in previous studies that investigated various post-processing treatments.[24,33]

To clarify the effect of the heat treatment parameters on the Si particles, the data obtained from digital image analysis were statistically evaluated, and the results are shown in Figure 7 and Table II.

Table II shows that the area fractions of the Si particles are quite similar regardless of the heat treatment, whereas the particle density is significantly lower after HIP + T6 treatment than after HPT6 and T6 treatment. Thus, the Si particles in the HIP + T6 sample are larger but less abundant. This is reasonable because in this case, the material is maintained for a longer time at a high temperature (520 °C). Moreover, the obtained values are in good agreement with previous studies on similar alloys.[13]

The equivalent diameter of the Si particles was also evaluated. In this context, it is well known that the Si particle size follows a two-parameter lognormal distribution.[41] This was verified in the present study, as shown in Figure 7, where the lognormal probability density function was used to fit the experimental data for the equivalent diameter obtained by digital image analysis. The shape parameter μ and scale parameter σ were estimated, and the results are listed in Table III.

Interestingly, these parameters were found to be almost identical for the HPT6 and T6 samples. This demonstrates that the coarsening of the Si particles, as measured in terms of the size distribution, is not significantly affected by the application of high pressure, which is the only parameter that differs in the treatment of the HPT6 and T6 samples.

By contrast, the lognormal curve of the HIP + T6 sample is wider and shifted toward higher values of the equivalent diameter. This is consistent with the literature on the coarsening of Si particles with increasing solution time.[42] In conclusion, the solution soaking time and temperature are the key parameters explaining the different evolution of the Si particle distribution and size, whereas the furnace pressure had a negligible effect in the studied range (0.1 to 150 MPa).

This is particularly relevant because increasing pressure is reportedly responsible for a change in the diffusivity of atoms in the Al matrix.[43] According to References 43 and 44, high pressure results in an increase in the Gibbs free energy associated with vacancy migration. In a substitutional solid solution, where diffusion phenomena are mediated by vacancies, this results in a lower diffusion coefficient,[45] and thus in the inhibition of diffusion phenomena. Furthermore, this increase in the Gibbs free energy also depends on the size of the substitutional atom, because it is a function of its atomic volume, as well as the pressure.[43] A reduction in diffusion phenomena due to an increase in pressure was recently documented in a study comparing the evolution of Si particles in a sand-cast AlSi7Mg alloy after HIP and vacuum treatment.[30]

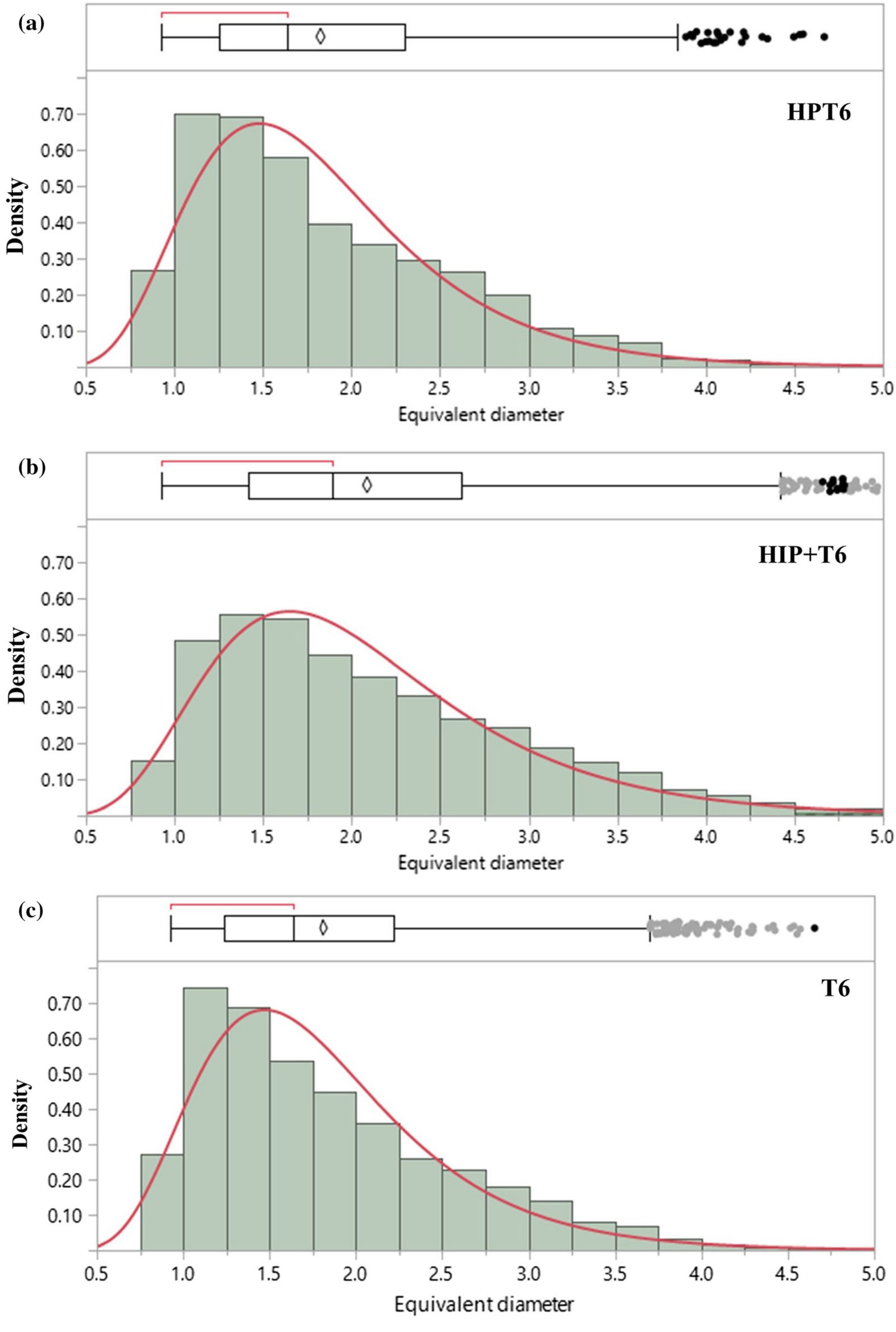

Fig. 7—Distributions of equivalent diameter of Si particles (histogram) and fitting with two-parameter lognormal distribution (red curve) for (*a*) HPT6, (*b*) HIP + T6, and (*c*) T6 samples.

Table II. Area Fraction and Particle Density of Si Particles After the Studied Heat Treatments

Sample Condition	Area Fraction (Pct)	Particles Density (Particles/mm^2)
HPT6	17.6	63×10^3
HIP + T6	16.5	41×10^3
T6	18.5	59×10^3

This difference between the results reported in Reference 30 and those of the present study can be explained in terms of the different microstructure of the alloys before treatment, *i.e.*, the as-built condition. In the sand-cast AlSi7Mg alloy, eutectic Si particles were significantly coarser and not as uniformly distributed as in the AlSi10Mg alloy produced by AM. Furthermore, the additively manufactured AlSi10Mg alloy underwent very rapid solidification, which allowed the formation of a supersaturated solid solution after production. Consequently, the Si atoms were already in solid solution and had to travel shorter distances for the Si particles to become coarse in the alloy studied here than in the sand-cast alloy. Thus, the decrease in the diffusion coefficient due to high pressure was less critical for the coarsening of the Si particles at the applied temperature (520 °C) and soaking time (2 hours). At lower temperatures or shorter soaking times, the coarsening of Si particles would likely be more sensitive to the decrease in diffusion coefficient caused by high pressure.

Regarding the effect of the heat treatments on the material density, the results in Figure 8(a) demonstrate that HIP treatment is effective for material densification when followed by either aging treatment at high pressure or conventional T6 treatment. The slightly lower density of the HIP + T6 samples compared with the HPT6 samples may be due to regrowth of gas pores, which are not perfectly closed during high temperature heat treatment, as reported for a Ti-based alloy.[23]

By contrast, as expected, annealing and T6 treatment without previous HIP cause a remarkable increase in the porosity, as the material density is significantly lower than that in the as-built samples.

Table III. Estimated Parameters for Two-Parameter Lognormal Distribution of Equivalent Diameter After Each Type of Heat Treatment

Sample Condition	μ (−)	σ (−)
HPT6	0.5315	0.3735
HIP + T6	0.6575	0.3964
T6	0.5235	0.3721

As discussed in a previous paper by the authors,[13] it is not possible to identify a direct relationship between the density and hardness, because other microstructural features also have to be taken into account (precipitation hardening of Mg_2Si particles, Si particles, grain size, *etc.*). This is confirmed by the present study. In fact, the hardness of the HPT6, HIP + T6, and T6 samples (Figure 8(b)) is significantly lower than that in the as-built samples owing to the microstructural changes that occurred during heat treatment. Among these samples, the HIP + T6 samples exhibited the highest hardness, despite their coarser Si particles, suggesting more effective hardening during aging treatment than under the other conditions. HPT6 treatment ensures a slightly higher hardness than conventional T6 treatment.

The discussion above indicates that the pressure during solution treatment cannot significantly affect the main microstructural features of the alloy.

Regarding the precipitation of Mg_2Si particles, a lower diffusion rate can be considered desirable because it delays the precipitation sequence and therefore the coarsening of the precipitates,[30] in comparison with aging treatment performed at atmospheric pressure. This does not contradict the previous discussion, because the lower temperature (165 °C) provides little energy for atomic motion compared with the first step (solution treatment at 520 °C). Therefore, HPT6 treatment can be considered to result in more effective precipitation strengthening of Mg_2Si particles. This can explain the higher hardness compared with that of the T6 sample, together with the higher density of the HPT6 sample. By contrast, the HIP + T6 sample shows the highest hardness owing to both effective densification during HIP and hardening due to successful aging treatment.

Finally, regarding the effect of heat treatment on grain size, it was demonstrated by Kan *et al.*[22] that no significant coarsening of grains takes place during T6 treatment or HIP. Therefore, it is considered that this parameter is not critical in the change in material performance after various heat treatments in comparison with as-built condition.

Figure 9 shows the density of tensile samples measured after machining. The density decreases strongly after T6 treatment, while HIP ensures that density

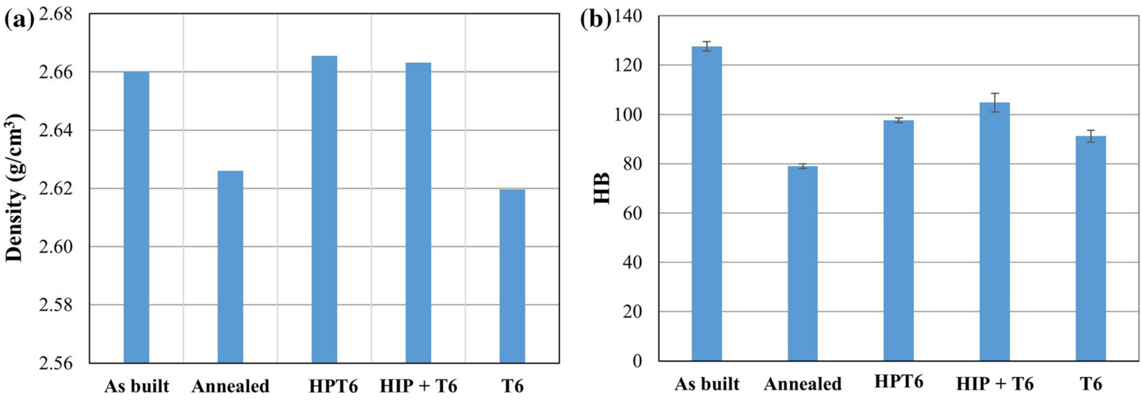

Fig. 8—(*a*) Density and (*b*) hardness of cubic samples.

values very similar to the material under as-built condition are maintained. Annealing reduces the density slightly, as also found by Reference 46. The effect of the sample geometry on the density can be clearly observed by comparing samples built in the horizontal and vertical directions (Figure 9). In fact, the as-built horizontal tensile samples have a higher density than the samples built in the vertical direction. This is reasonable because the effects of the geometry, size, and orientation on the porosity are well documented,[47–50] and this is important for the design of real components. In particular, the variation in the density of the as-built samples is likely due to differences in the formation of H_2 pores, which is enhanced by the longer time spent at high temperature during AM processing of vertical samples compared to horizontal samples, according to the geometry and building orientation.[51] The same overall trend in the density can be observed for the heat-treated cubic and tensile samples.

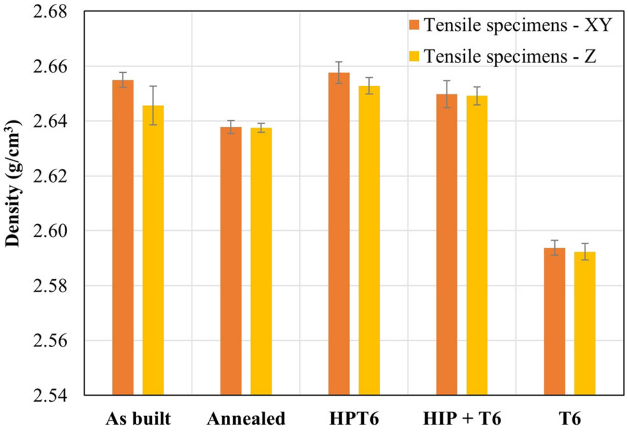

Fig. 9—Density of tensile samples.

The tensile properties of the samples built in the horizontal direction are summarized in Table IV. As expected, the as-built material exhibits remarkable strength and good elongation. Annealing sharply decreases the material strength, whereas it slightly increases the ductility.

The other studied heat treatments cause decreases in both the UTS and elongation, whereas the YS values are similar or even slightly higher because of matrix precipitation hardening. These findings are in agreement with various studies.[24,52] Interestingly, however, the HPT6 treatment produces the highest elongation among the age-hardened samples, whereas the UTS is comparable to that of the T6 samples and slightly lower than that of the HIP + T6 samples. This is consistent with the hardness results presented above (Figure 8(b)); HIP + T6 treatment leads to better hardening of the material than the HPT6 route, which in turn ensures higher ductility.

The properties of the samples built in the vertical direction are different (Table V). The strength in the as-built condition is again very high, whereas the elongation is quite limited. This can be linked to the coarser melt pool boundary of the studied alloy (Figure 3(a)), which is a preferential site for crack propagation when the material is loaded along the building direction. This is well documented.[25,39,53] In particular, Xiong *et al.*[39] demonstrated that the melt pool boundaries play a more significant role during tensile loading and fracture propagation than the grain texture. Furthermore, Girelli *et al.*[25] found that the interlayer boundary is weaker that the intertrack boundary during impact loading. This is also demonstrated by SEM observation of the fracture surface (Figure 11(a)), where the scan track profiles are evident. On the other hand, Young's modulus appears not to be strongly affected by the two building directions considered in the present study. This is in agreement with

Table IV. Mechanical Properties and Relative Density of Samples Built in Horizontal Direction

	E (GPa)	YS (MPa)	UTS (MPa)	El (Pct)	Relative Density (Pct)
As Built	66.7 ± 1.9	251 ± 6	409 ± 6	7.7 ± 0.4	99.1 ± 0.1
Annealed	63.3 ± 1.2	151 ± 6	245 ± 3	7.8 ± 0.3	98.4 ± 0.1
HPT6	67.2 ± 1.9	252 ± 6	306 ± 4	6.4 ± 0.6	99.2 ± 0.1
HIP + T6	69.2 ± 0.7	261 ± 2	313 ± 2	5.9 ± 0.2	98.9 ± 0.2
T6	65.1 ± 1.3	258 ± 2	305 ± 5	3.8 ± 0.2	96.8 ± 0.1

Table V. Mechanical Properties and Relative Density of Samples Built in Vertical Direction

	E (GPa)	YS (MPa)	UTS (MPa)	El (Pct)	Relative Density (Pct)
As built	67.5 ± 2.6	262 ± 7	431 ± 12	4.7 ± 0.4	98.7 ± 0.3
Annealed	60.6 ± 2.0	157 ± 5	258 ± 2	6.2 ± 0.4	98.4 ± 0.1
HPT6	69.3 ± 0.4	252 ± 1	306 ± 1	6.4 ± 0.4	99.0 ± 0.1
HIP + T6	70.9 ± 0.3	258 ± 12	309 ±10	6.5 ± 1.3	98.8 ± 0.1
T6	65.8 ± 0.9	242 ± 1	289 ± 4	5.4 ± 0.8	98.4 ± 0.1

Reference 54 where it is shown that only certain orientations are critical for the Young's modulus, while it keeps quite constant in most cases.

Finally, also the role of lack-of-fusion porosity, which usually are elongated normal to the building direction, has to be considered. The presence of these defects is more critical for vertically built samples than that of the horizontally built ones.[24] In fact, due to their orientation, lack-of-fusion porosities are normal to the loading direction for vertical samples, significantly reducing the load bearing section and contributing to their lower ductility, as also well discussed in Reference 24.

In this case, all the heat treatments enhanced the ductility, especially those performed at high pressure, probably owing to the lower porosity.[27] In particular, the innovative HPT6 treatment resulted in performance very similar to that achieved after HIP + T6 treatment. In fact, the slight loss of strength and hardness is balanced by the good ductility. These results from tensile tests provide a first useful indication of the effectiveness of HPT6 treatment. It is worth noting that further testing under dynamic loading is necessary for a comprehensive evaluation of material performance and HPT6 advantages. In fact, the presence of porosities, especially if close to the external surface can be particularly critical for fatigue resistance.

Fracture surface analysis (Figures 10 and 11) confirms that several pores are visible in the as-built, annealed, and T6 samples (Figures 10(a) and (b) and 11(a) and (b)), whereas they are rare in the HIPed materials (Figures 10(c) and (d) and 11(c) and (d)). In the as-built and annealed samples, the pores are small

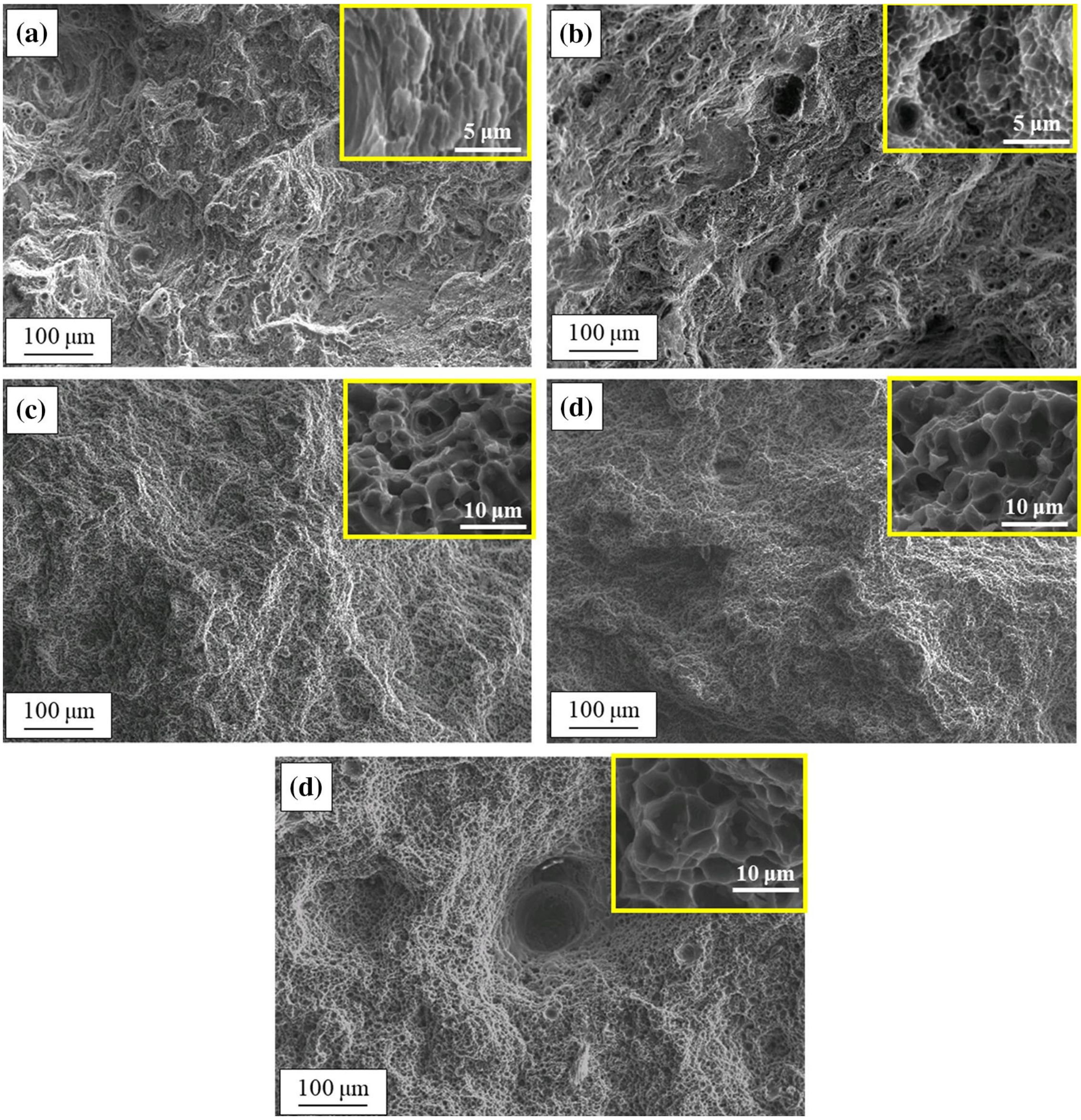

Fig. 10—Fracture surfaces of samples built in horizontal direction: (*a*) as-built, (*b*) annealed, and after (*c*) HPT6, (*d*) HIP + T6, and (*e*) T6 treatment. Magnification is given in the box.

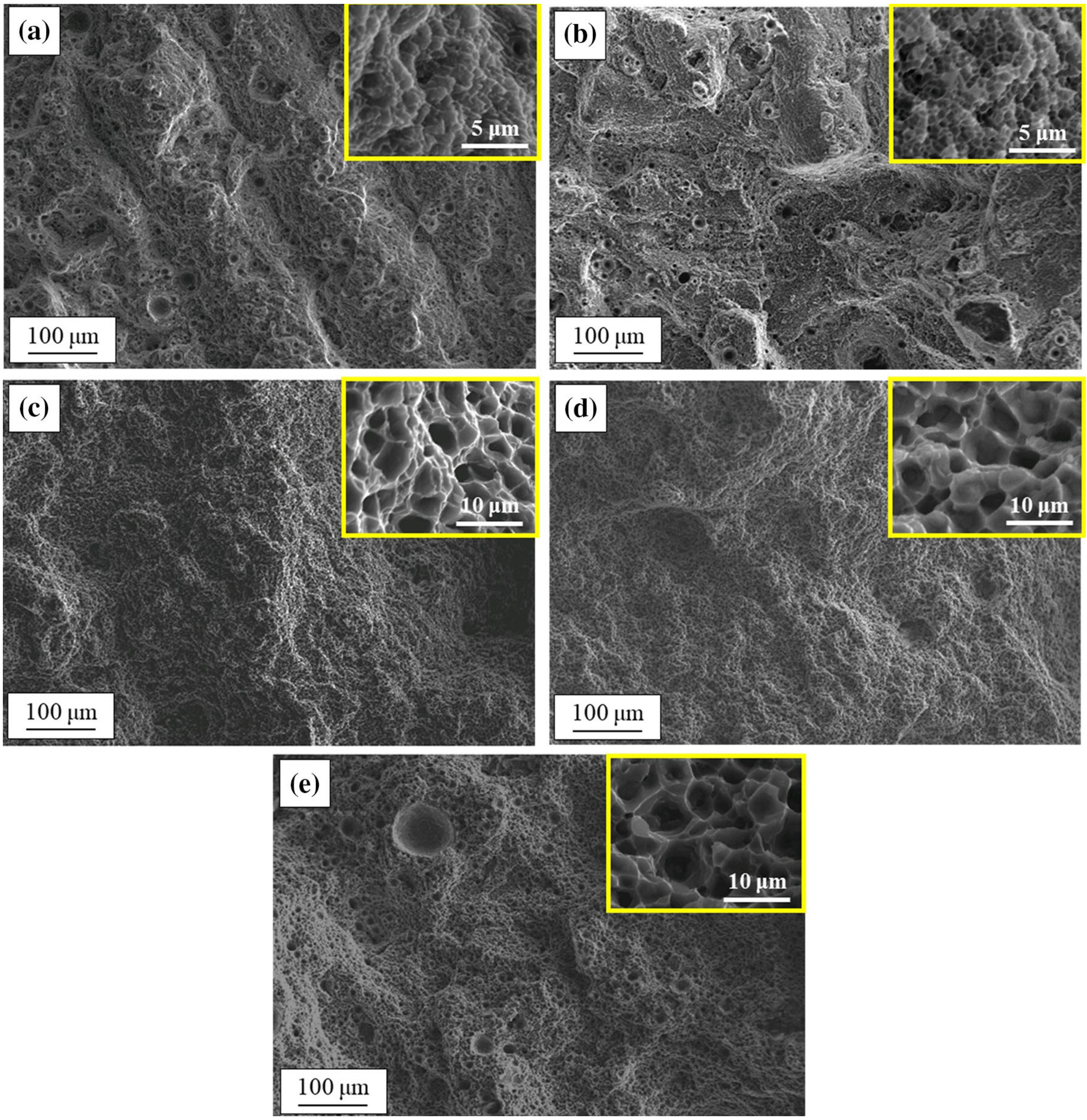

Fig. 11—Fracture surfaces of samples built in vertical direction: (*a*) as-built, (*b*) annealed, and after (*c*) HPT6, (*d*) HIP + T6, and (*e*) T6 treatment.

and very abundant on the fracture surface (Figures 10(a) and (b) and 11(a) and (b)), whereas in the T6 sample, they are fewer but much larger, which degrades the mechanical properties of the sample (Figures 10(e) and 11(e)). For all the heat-treated samples, the fracture mechanism is mainly ductile, as demonstrated by the formation of microdimples, which are visible at higher magnification in the insets of Figures 10 and 11. The dimple sizes of the age-hardened samples are also comparable.

Scan track profiles are particularly evident on the fracture surfaces of samples built in the vertical direction (Figure 11(a)). As mentioned above, this can explain why these samples have lower ductility than those built in the horizontal direction. After annealing, the scan track boundaries become less visible, although some can still be identified, probably because of the limited soaking time (Figure 11(b)). This also explains the limited gain in elongation for this sample compared with those treated under other conditions.

IV. CONCLUSIONS

The effect of a high-pressure T6 heat treatment (HPT6) was evaluated in terms of the densification and improvement of the mechanical properties. The treatment was found to ensure high density, comparable to or even higher than that obtained by conventional HIP treatment. The effect of pressure on the coarsening of Si particles was demonstrated to be negligible, as revealed by the equivalent diameter, area fraction, and density of the Si particles, whereas these parameters are affected by the total soaking time at high temperature. Furthermore, the HPT6 samples exhibited significant strength and good elongation, although their hardness was slightly lower than that obtained by HIP + T6 treatment. However, the reduced time required for the HPT6 one-step cycle represents a key advantage over the HIP + T6 route; therefore, it can be considered an interesting alternative to ensure high densification and improved mechanical properties for high-performance applications.

ACKNOWLEDGMENTS

The authors gratefully acknowledge Dr J. Shipley and Dr J. Gårdstam (Quintus Technologies AB) for HIP treatments, Dr L. Girelli for support during the experimental design, Dr L. Montesano for SEM analysis, and Mr A. Al Mawali for help with sample preparation and testing.

REFERENCES

1. L. Murr, S. Gaytan, D. Ramirez, E. Martinez, J. Hernandez, K. Amato, P. Shindo, F. Medina, and R. Wicker: *J. Mater. Sci. Technol.*, 2012, vol. 28 (1), pp. 1–14.
2. D. Herzog, V. Seyda, E. Wycisk, and C. Emmelmann: *Acta Mater.*, 2016, vol. 117, pp. 371–92.
3. C. Yap, C. Chua, Z. Dong, Z. Liu, D. Zhang, L. Loh, and S. Sing: *Appl. Phys. Rev.*, 2015, vol. 2, no. 4, art. no. 041101.
4. N. Aboulkhair, N. Everitt, I. Ashcroft, and C. Tuck: *Addit. Manuf.*, 2014, vols. 1–4, pp. 77–86.
5. J. Martin, B. Yahata, J. Hundley, J. Mayer, T. Schaedler, and T. Pollock: *Nature*, 2017, vol. 549, pp. 365–69.
6. S. Sing, J. An, W. Yeong, and F. Wiria: *J. Orthop. Res.*, 2016, vol. 34 (3), pp. 369–85.
7. S.U.C. Scudino, K. Prashanth, H. Attar, N. Ellendt, V. Uhlenwinkel, and J. Eckert: *Mater. Lett.*, 2015, vol. 156, pp. 202–04.
8. R. Karunakaran, S. Ortgies, A. Tamayol, F. Bobaru, and M.P. Sealy: *Bioact. Mater.*, 2020, vol. 5, pp. 44–54.
9. N. Aboulkhair, M.P.L. Simonelli, I. Ashcroft, C. Tuck, and R. Hague: *Prog. Mater. Sci.*, 2019, vol. 106, art. no. 100578.
10. N. Aboulkhair, I. Maskery, C. Tuck, I. Ashcroft, and N. Everitt: *Mater. Sci. Eng. A*, 2016, vol. 667, pp. 139–46.
11. J. Wu, X. Wang, W. Wang, M. Attallah, and M. Loretto: *Acta Mater.*, 2016, vol. 117, pp. 311–20.
12. L. Thijs, K. Kempen, J.-P. Kruth, and J. Humbeeck: *Acta Mater.*, 2013, vol. 61, pp. 1809–19.
13. L. Girelli, M. Tocci, M. Gelfi, and A. Pola: *Mater. Sci. Eng. A*, 2019, vol. 739, pp. 317–28.
14. S. Chou, M. Trask, J. Danovitch, X. Wang, J. Choi, and M. Brochu: *Mater. Charact.*, 2018, vol. 143, pp. 27–33.
15. R. Casati, and M. Vedani: *Adv. Eng. Mater., 2019, vol.* 21, no. 4, art. no. 1800406.
16. A.B. Spierings, K. Dawson, K. Kern, F. Palm, and K. Wegener: *Mater. Sci. Eng. A*, 2017, vol. 701, pp. 264–73.
17. R. Casati, M. Coduri, M. Riccio, A. Rizzi, and M. Vedani: *J. Alloy Compd.*, 2019, vol. 801, pp. 243–53.
18. F. Kim, and S. Moylan: *Advanced Manufacturing Series (NIST AMS)*, 2018, report no. 100-16. https://doi.org/10.6028/nist.ams.100-16.
19. I. Maskery, N. Aboulkhair, M. Corfield, C. Tuck, A. Clare, R. Leach, R. Wildman, I. Ashcroft, and R. Hague: *Mater. Charact.*, 2016, vol. 111, pp. 193–204.
20. C. Weingarten, D. Buchbinder, N. Pirch, W. Meiners, K. Wissenbach, and R. Poprawe: *J. Mater. Proc. Technol.*, 2015, vol. 221, pp. 112–20.
21. S. Hojjatzadeh, N. Parab, W. Yan, Q. Guo, L. Xiong, C. Zhao, M. Qu, L. Escano, X. Xiao, K. Fezzaa, W. Everhart, T. Sun, and L. Chen: *Nat. Commun.*, 2019, vol. 10, art. no. 3088.
22. W. Kan, Y. Nadot, M. Foley, L. Ridosz, G. Proust, and J. Cairney: *Addit. Manuf*, 2019, vol. 29, art. no. 100805.
23. S. Tammas-Williams, P. Withers, I. Todd, and P. Prangnell: *Scr. Mater.*, 2016, vol. 122, pp. 72–76.
24. U. Tradowsky, J. White, R. Ward, N. Read, W. Reimers, and M. Attallah: *Mater. Des.*, 2016, vol. 105, pp. 212–22.
25. L. Girelli, M. Giovagnoli, M. Tocci, A. Pola, A. Fortini, M. Merlin, and G.M. La Vecchia: *Mater. Sci. Eng. A*, 2019, vol. 748, pp. 38–51.
26. I. Rosenthal, R. Shneck, and A. Stern: *Mater. Sci. Eng. A*, 2018, vol. 729, pp. 310–22.
27. C. Finfrock, A. Exil, J. Carrol, and L. Deibler: *Metall. Microstruct. Anal.*, 2018, vol. 7, pp. 443–56.
28. H. Atkinson and S. Davies: *Metall. Mater. Trans. A*, 2000, vol. 31A, pp. 2981–3000.
29. N. Uzan, R. Shneck, O. Yeheskel, and N. Frage: *Mater. Sci. Eng. A*, 2017, vol. 704, pp. 229–37.
30. S. Hafenstein and E. Werner: *Mater. Sci. Eng. A*, 2019, vol. 757, pp. 62–69.
31. A.H. Maamoun, M. Elbestawi, G. Dosbaeva, and S. Veldhuis: *Addit. Manuf.*, 2018, vol. 21, pp. 234–47.
32. S. Hafenstein, M. Brummer, M. Ahlfors, and E. Werner: *HTM J. Heat Treatm. Mater.*, 2016, vol. 71 (3), pp. 117–24.
33. L. Zhuo, Z. Wang, H. Zhang, E. Yin, Y. Wang, T. Xu, and C. Li: *Mater. Lett.*, 2019, vol. 234, pp. 196–200.
34. J.R. Davis (Ed.): *ASM Speciality Handbook, Aluminum and Aluminum Alloys*, ASM International, Davis & Associates, 1993.
35. D. Gu, F. Chang, D. Dai: *J. Manuf. Sci. Eng.*, 2015, vol. 137, art. no. 021010.
36. A. Aversa, M. Lorusso, G. Cattano, D. Manfredi, F. Calignano, E.P. Ambrosio, S. Biamino, P. Fino, M. Lombardi, and M. Pavese: *J. Alloy Compd.*, 2017, vol. 695, pp. 1470–78.
37. L. Lam, D. Zhang, Z. Liu, and C. Chua: *Virtual Phys. Prototyp.*, 2015, vol. 10, pp. 207–15.
38. X. Liu, C. Zhao, X. Zhou, Z. Shen, and W. Liu: *Mater. Des.*, 2019, vol. 168, art. no. 107677.
39. Z. Xiong, S. Liu, S. Li, Y. Shi, Y. Yang, and R. Misra: *Mater. Sci. Eng. A*, 2019, vols. 740–741, pp. 148–56.
40. J. Fiocchi, A. Tuissi, P. Bassani, and C. Biffi: *J. Alloy Compd.*, 2017, vol. 695, pp. 3402–09.
41. M. Tiryakioğlu: *Mater. Sci. Eng. A*, 2008, vol. 473 (1–2), pp. 1–6.
42. G. Eisaabadi, G. Yeom, M. Tiryakioğlu, N. Netto, R. Beygi, M. Mehrizi, and S. Kim: *Mater. Sci. Eng. A*, 2018, vol. 722, pp. 1–7.
43. H. Mehrer: *Diffusion in Solids—Fundamentals, Methods, Materials, Diffusion-Controlled Processes*, 1st ed., Springer, Berlin, 2007, pp. 132–40.
44. J. Sobczak, L. Drenchev, and R. Asthana: *Int. J. Cast Metal. Res*, 2012, vol. 25 (1), pp. 1–14.
45. T. Yamane, N. Mori, Y. Minamino, Y. Miyamoto, M. Koizumi, and T. Takahashi: *Metall. Trans. A*, 1988, vol. 19, pp. 467–71.
46. P. Yang, L.A. Deibler, D.R. Bradley, D.K. Stefan, and J.D. Carroll: *J. Mater. Res.*, 2018, vol. 33, pp. 4040–52.
47. Z. Dong, Y. Liu, W. Li, and J. Liang: *J. Alloy Compd.*, 2019, vol. 791, pp. 490–500.
48. N. Larrosa, W. Wang, N. Read, M. Loretto, C. Evans, J. Carr, U. Tradowsky, M. Attallah, and P. Withers: *Theor. Appl. Fract. Mech.*, 2018, vol. 98, pp. 123–33.
49. F. Léonard, S. Tammas-Williams, P. Prangnell, I. Todd, and P. Withers, *Conf. Ind. Comput. Tomogr.*, 2012, pp. 85–93, http://www.ndt.net/article/ctc2012/papers/91.pdf.
50. Z. Dong, X. Zhang, W. Shi, H. Zhou, H. Lei, and J. Liang: *Materials*, 2018, vol. 11, art. no. 2463.
51. P. Delroisse, P. Jacques, E. Maire, O. Rigo, and A. Simar: *Scr. Mater.*, 2017, vol. 141, pp. 32–35.
52. L. Zhou, A. Mehta, E. Schulz, B. McWilliams, K. Cho, and Y. Sohn: *Mater. Charact.*, 2018, vol. 143, pp. 5–17.

53. D. Dai, D. Gu, H. Zhang, J. Xiong, C. Ma, C. Hong, and R. Poprawe: *Opt. Laser Technol.*, 2018, vol. 99, pp. 91–100.
54. L. Hitzler, C. Janousch, J. Schanz, M. Merkel, B. Heine, F. Mack, W. Hall, and A. Ochsner: *J. Mater. Proc. Technol.*, 2017, vol. 243, pp. 48–61.